

Size-restricted magnetotransport in the delafossite metals PdCoO₂ and PtCoO₂

M. Moravec^{1,2}, G. Baker^{1, *}, M.D. Bachmann¹, A.L. Sharpe^{3,4}, N. Nandi¹, A.W. Barnard⁵, C. Putzke⁶, S. Khim¹, M. König¹, D. Goldhaber-Gordon^{3,4}, P.J.W. Moll⁶, and A.P. Mackenzie^{1,2, †}

¹ Max Planck Institute for Chemical Physics of Solids, Dresden, Germany

² Scottish Universities Physics Alliance, School of Physics and Astronomy, University of St Andrews, St Andrews, UK

³ Department of Physics, Stanford University, Stanford, CA, USA

⁴ Stanford Institute for Materials and Energy Sciences, SLAC National Accelerator Laboratory, Menlo Park, CA, USA

⁵ Department of Physics, University of Washington, Seattle, WA, USA

⁶ Department of Materials Science and Engineering, University of Washington, Seattle, WA, USA

⁷ Max Planck Institute for the Structure and Dynamics of Matter, Hamburg, Germany

Abstract

Studies of electronic transport in width-restricted channels of PdCoO₂ have recently revealed a novel ‘directional ballistic’ regime, in which ballistic propagation of electrons on an anisotropic Fermi surface breaks the symmetries of bulk transport. Here we introduce a magnetic field to this regime, in channels of PdCoO₂ and PtCoO₂ along two crystallographically distinct directions and over a wide range of widths. We observe magnetoresistance distinct from that in the bulk, with features strongly dependent on channel orientation and becoming more pronounced the narrower the channel. Comparison to semi-classical theory establishes that magnetoresistance arises from field-induced modification of boundary scattering, and helps connect features in the data with specific electronic trajectories. However, the role of bulk scattering in our measurements is yet to be fully understood. Our results demonstrate that finite-size magnetotransport is sensitive to the anisotropy of Fermi surface properties, motivating future work to fully understand and exploit this sensitivity.

*graham.baker@cpfs.mpg.de

†andy.mackenzie@cpfs.mpg.de

Introduction

The delafossite metals PdCoO₂, PtCoO₂, and PdCrO₂ [1] have become known as benchmarks for studying quasi two-dimensional electrical transport in the limit of extremely high conductivity [2]. Mean free paths ranging from several microns to over twenty microns have been observed in bulk crystals [3–8], due to the extremely high crystal quality in the conducting Pd or Pt planes [9], and the screening of out-of-plane impurity potentials [8,10]. Due to the long mean free paths, they are ideal for study of the de Haas-van Alphen effect (dHvA) [3,11–13], and due to their quasi two-dimensionality they yield excellent angle-resolved photoemission spectroscopy (ARPES) data [14–19].

Together, the dHvA and ARPES establish that PdCoO₂ and PtCoO₂ have nearly cylindrical Fermi surfaces with pronounced faceting that gives them almost hexagonal cross-sections. The triangular symmetry of the conducting planes means that the bulk in-plane resistivity is isotropic, but if transport is studied in samples restricted in one or more dimensions to length scales of order the mean free path, pronounced directional effects can be observed due to the bulk symmetry being broken by the shape of the sample. The delafossites are chemically suitable for focused ion beam (FIB) micro-structuring, which has enabled a series of experiments studying these directional effects as well as quantum coherence over length scales of over ten microns [20–25]. Width restriction can also be achieved by tuning the skin depth in frequency-dependent electrodynamic studies [10], and the effect of Fermi surface faceting is the subject of active theoretical research [26–28].

Our goal in this paper is to report a comprehensive study of directional effects on the transverse magnetoresistance of width-restricted channels of PdCoO₂ and PtCoO₂. Size-restricted magnetotransport in this geometry¹ has received considerable theoretical attention [29–36], and has been studied experimentally in elemental metals [29], graphene [37], and GaAs [36,38,39]. However, these works have focussed on materials in which the Fermi surface is well-approximated as isotropic. While this geometry was also studied in PdCoO₂ [40], at the time the importance of directional effects in PdCoO₂ was not appreciated, so the channels were not aligned with the crystallographic axes. Since then, large directional effects have been reported in this geometry in zero magnetic field [22,25], but not over a wide range of widths.

Here, we report on the effect of magnetic fields on transport in a single PdCoO₂ device incorporating channels cut along the in-plane a axis (previously established as the low-resistance, or ‘easy’ transport direction) and at 30° to it (the ‘hard’ direction). Each channel was studied, then narrowed, in an iterative procedure that built up a large data set. In the main manuscript we concentrate on reporting the properties of this single device, but in supplementary information we show additional data sets from other PdCoO₂ and PtCoO₂ devices, demonstrating the consistency of the main trends that we identify in the data. We complement the experimental data with the results of Boltzmann calculations and Monte Carlo simulations for both idealized and realistic Fermi surface geometries. Our

¹By “transverse magnetoresistance in width-restricted channels”, we mean a geometry in which current, magnetic field, and size-restricted dimension are all along mutually perpendicular directions. This is as opposed to “transverse magnetoresistance of thickness-restricted channels”, in which magnetic field is perpendicular to current but parallel to the size-restricted dimension. The latter situation has also been studied theoretically and experimentally [47], but is conceptually and phenomenologically distinct from the present geometry.

measurements and analysis demonstrate how this experimental arrangement can be used to study the anisotropy of Fermi surface geometry and scattering.

Results

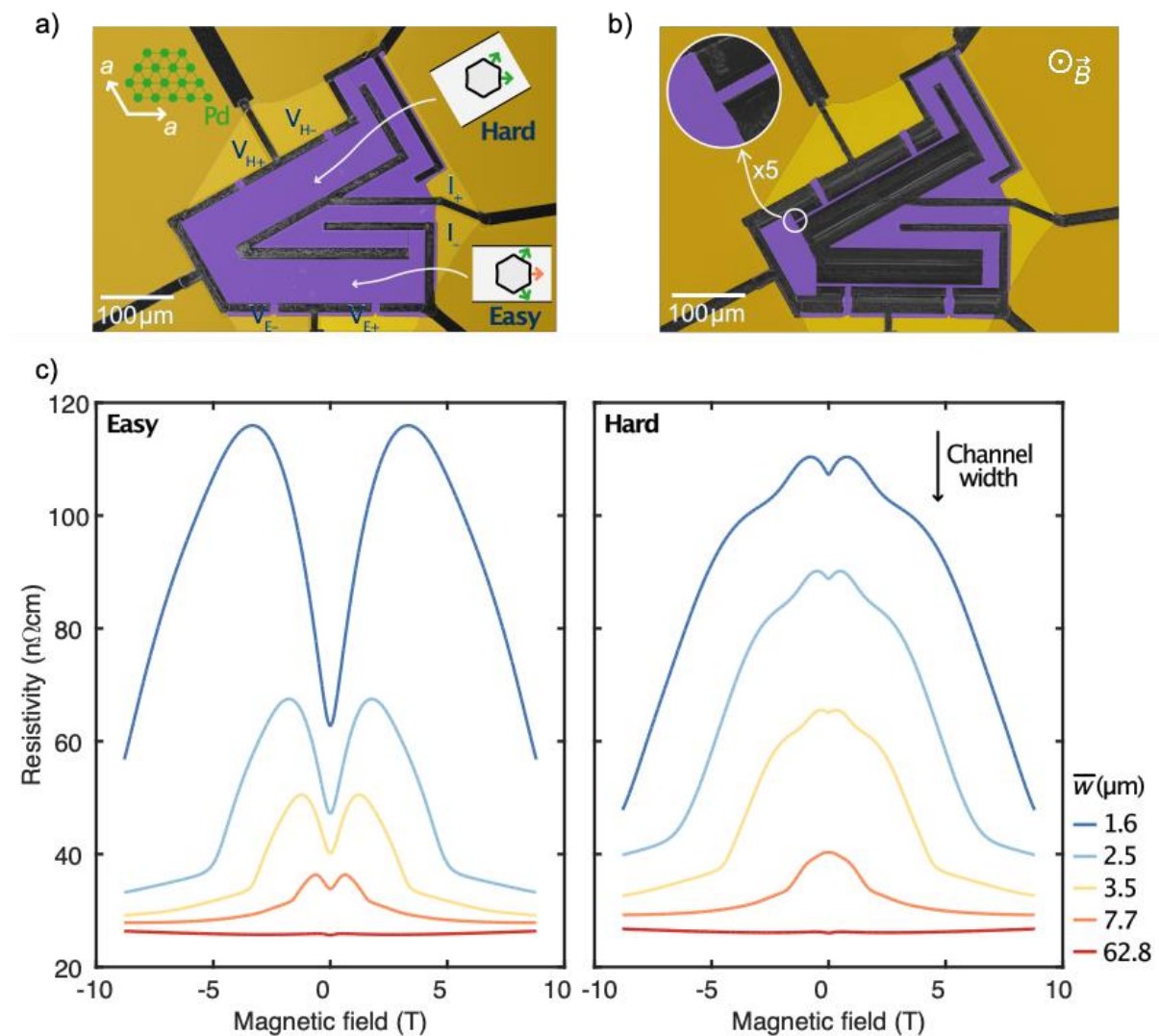


Figure 1. (a) False-colour scanning electron micrograph of the starting PdCoO₂ device S1 for our experiment. Current is injected through gold contacts on the top of a single crystal of PdCoO₂ and then flows through meander tracks to become homogeneous through the thickness of the sample before flowing through two conducting channels cut at 30° to one another. These are oriented relative to the Fermi surface facets in the so-called ‘hard’ and ‘easy’ directions previously identified in studies of directional transport in PdCoO₂ in zero applied magnetic field [22], and are 63 μm wide. (b) The same device after successive FIB narrowing to a channel width of 3.5 μm. (c)(d) Magnetoresistance data for five channel widths along the easy and hard directions respectively. The legend shows the average of the channel widths in the two directions, \bar{w} .

A device (S1) used for our experiment is shown in the micrographs of Fig. 1 (a) and (b). A single crystal of PdCoO₂ 1.8 μm thick is sculpted using a focused ion beam into two conducting channels along the hard and easy directions identified in [22]. Initially the width, w , of each channel was 63 μm. Magnetoresistance was measured, and then the conducting channels were narrowed, in 18 steps, to 0.75 μm, with the magnetoresistance measured along both directions at each step. To ensure the reliability of the experiment, considerable care must be taken to select crystal platelets of uniform thickness, and to maintain the width

and separation of the voltage contacts on each channel. With the main crystal selection criterion being uniformity rather than the lowest attainable resistivity, the crystal shown in Fig. 1 had a residual resistivity of 26 nΩ cm, approximately a factor of three higher than those attainable in the purest PdCoO₂ [6,22,40].

Resistivity data from S1 are shown in Fig. 1 (c) and (d). The easy-direction data shown in 1 (c) are qualitatively similar to those reported in Ref. [40] (for which the channel direction was not aligned precisely with a crystal axis) but those from the hard direction are qualitatively different. In both cases, the zero-field resistivity grows as the channel is narrowed, due to an increasing influence of boundary scattering, with the zero-field resistivity along the hard direction significantly larger than that along the easy direction for channels of similar width. There are then resistivity maxima as the field is increased, before the resistivity falls with increasing fields. The functional form of the magnetoresistance is clearly different for the two directions, but several features common to all the curves can be identified. Firstly, there is structure in the curves (the maxima and then pronounced kinks at higher fields) that scale approximately with field magnitude. Secondly, at high magnetic fields the hard and easy direction data look more similar to each other than at low fields, and seem to be tending to the value of the resistivity of the broadest sample. Both of these observations are consistent with a sufficiently high field cutting off the boundary-induced back-scattering, and point to the likely significance of the dimensionless ratio w/r_c to the phenomenology of the problem, where we define an average cyclotron radius $r_c = \hbar \bar{k}_F / eB$, with \hbar the reduced Planck's constant, e the electron charge, and \bar{k}_F the average Fermi momentum (defined in the Methods section).

A third length scale of relevance to the observations is the resistive mean free path λ , which is a measure of the relaxation of electron momentum through bulk scattering events. It can be changed either by varying sample purity or by raising the temperature to introduce phonon scattering. In each case, doing so reduces both the overall scale of the magnetoresistance and its anisotropy, as shown in the Supplementary Information. This is unsurprising because the stronger the bulk scattering, the weaker the relative influence of boundary scattering for a given value of w/r_c .

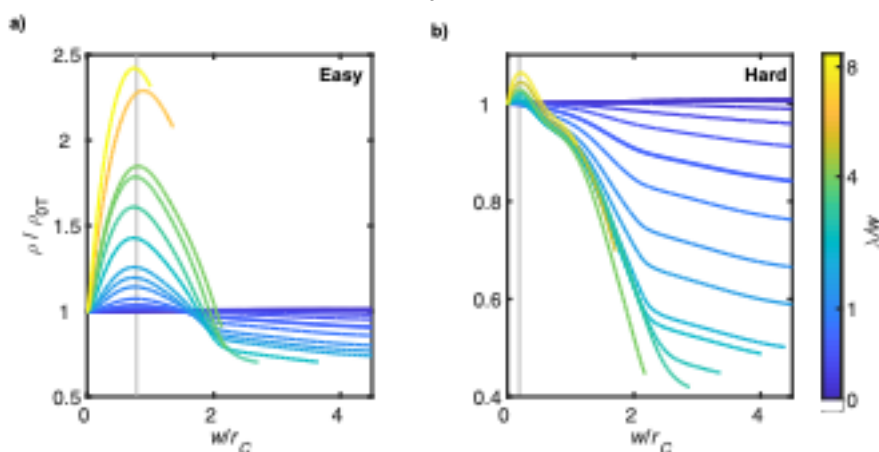


Figure 2. The complete data set for PdCoO₂ S1, plotted along (a) the easy and (b) the hard directions. For each channel width, resistivity data are normalized to the value at zero field, with the value of λ/w indicated by the colour of the trace. Data are plotted against a second dimensionless variable, w/r_c . The vertical, grey lines

mark the average position of the peak in magnetoresistance, at $w/r_c = 0.78$ and 0.19 for the easy and hard orientations, respectively.

In order to examine the trends identified in the discussion of Fig. 1, we show in Fig. 2 the resistivity at each width w , normalized to the zero-field resistivity at that width, plotted against w/r_c . The normalization removes the effect of width-dependent boundary scattering at zero-field and instead emphasizes the relative influence of the magnetic field on boundary scattering. The colour of the traces represents the value of λ/w , emphasizing that the overall scale of the magnetoresistance has a clear systematic dependence on this dimensionless ratio.

The main field-dependent features seen in Fig. 1 do indeed occur at the same values of w/r_c , and the reduction of the resistivity in narrow channels from its zero-field value at sufficiently high w/r_c is highlighted. For the easy direction, the peak in the magnetoresistance occurs at $w/r_c \approx 0.6$, similar to a previous observation [40], while for the hard direction the overall maximum occurs at much smaller w/r_c , followed by a shoulder feature. In both orientations, a kink in the data is visible at $w/r_c \approx 2$.

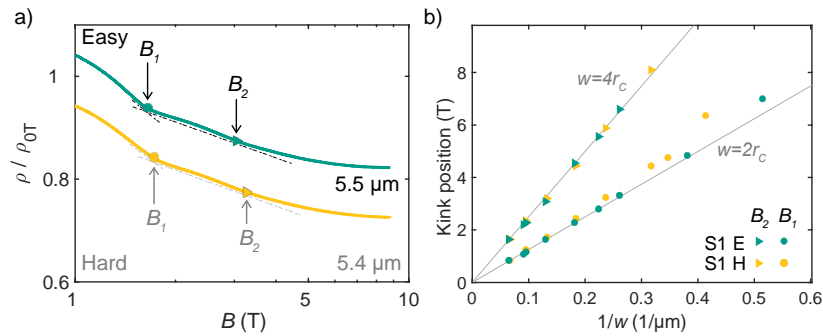


Figure 3. Plotting the magnetoresistance against magnetic field on a semi-log scale reveals the existence of two kinks in the data at characteristic fields B_1 and B_2 for both easy and hard direction transport (a and b). c) Plotting B_1 and B_2 for samples with a wide range of widths against $1/w$ reveals that they correspond approximately to $w = 2r_c$ and $w = 4r_c$ respectively. In the data for B_1 , a small systematic difference between the easy and hard directions is resolved, with the hard direction kink corresponding to w slightly greater than $2r_c$.

To investigate the kink at $w/r_c \approx 2$ in more detail, we plot data from a representative width of approximately $5.5 \mu\text{m}$ in Fig. 3 on a semi-log plot. This reveals that we in fact resolve two kinks, the second at approximately twice the field of the first. Identifying the kinks via local maxima in $\partial^2\rho/\partial B^2$ (as described in the Supplementary Information) across samples with a range of widths for which they are accessible in the 9 T magnet used to study S1, we observe that they are indeed consistently observed at approximately $2r_c$ and $4r_c$ respectively, as shown in Fig. 3c).

In addition to the data presented in Figs. 1–3, comprehensive measurements from two additional PdCoO_2 samples as well as two PtCoO_2 samples are presented in the Supplementary Information. The data from all samples of a given material are fully consistent with one another, and the trends identified here for PdCoO_2 are also seen in PtCoO_2 . The comparison is discussed further in the Supplementary Information.

Discussion

To set the context for our discussion, we summarize the set of experimental features, established in Figures 2 & 3, with which our analysis must contend. At low magnetic fields, the data show a rapid rise and then fall as magnetic field is increased. The form and magnitude of this behaviour differ significantly between the two channel orientations. For a given channel orientation, the position of the magnetoresistance peak appears to occur at a set value of w/r_c , and its magnitude increases as the ratio λ/w is increased. At high fields, the resistivity decreases with increasing magnetic field, displaying two kinks at which the slope of this behaviour changes. The second kink appears to always occur at $w/r_c = 4$, while the first kink occurs near $w/r_c = 2$ but with a precise value that is systematically different between channel orientations. In all cases, the kinks become more pronounced with increasing λ/w .

Considering the semi-classical electron dynamics underlying our experiment helps suggest the key ingredients for understanding this set of features. For a magnetic field along the c axis in PdCoO₂, the in-plane semi-classical trajectories in a perfect, infinite lattice are closed cyclotron orbits. The real-space shape of the in-plane cyclotron orbits is the same as that of the hexagonal Fermi surface but rotated by 90°, and the size of the orbits is scaled by the magnetic field according to $r_c = \hbar \bar{k}_F / eB$.² In a real, finite lattice, scattering at the sample's boundaries and in its bulk acts to interrupt the cyclotron motion.

A theoretical model suitable for quantitatively analysing the full set of experimental features would need to incorporate Fermi surface anisotropy, scattering at the sample's boundaries, and scattering in the sample's bulk. To our knowledge, such a complete model does not currently exist. However, we believe that the experimental feature set can be understood at a qualitative level via a multi-pronged approach. This is enabled by the fact that feature locations depend on w/r_c while their magnitude depends on λ/w .

At low fields with $w/r_c < 2$, the data are strongly dependent on channel orientation. To analyze the role of Fermi surface geometry on the w/r_c -dependence of the resistivity, we performed Boltzmann calculations taking into account boundary scattering and a realistic Fermi surface geometry, but in the simplifying limit of no bulk scattering. (In the Supplementary Information, we also show the results of Monte Carlo simulations for the same set of assumptions.) At high fields with $w/r_c > 2$, the data is more isotropic. Here we make geometrical arguments about different orbits and their contribution to resistivity to explain the occurrence of kinks at $w/r_c \approx 2$ and $w/r_c = 4$, which are supported by previous numerical calculations for a circular Fermi surface [36]. In both regimes, we then rely on qualitative arguments to explain how the magnitude of these features depends on bulk scattering, as quantified by the ratio λ/w .

²These statements apply to the in-plane motion, i.e. the projection of the real-space motion in the plane perpendicular to the c -axis magnetic field. The c -axis velocity is a constant of motion and the three-dimensional real-space path is in fact helical. However, the c -axis velocity is orders of magnitude smaller than the in-plane velocity, and so we do not consider the c -axis motion in our analysis.

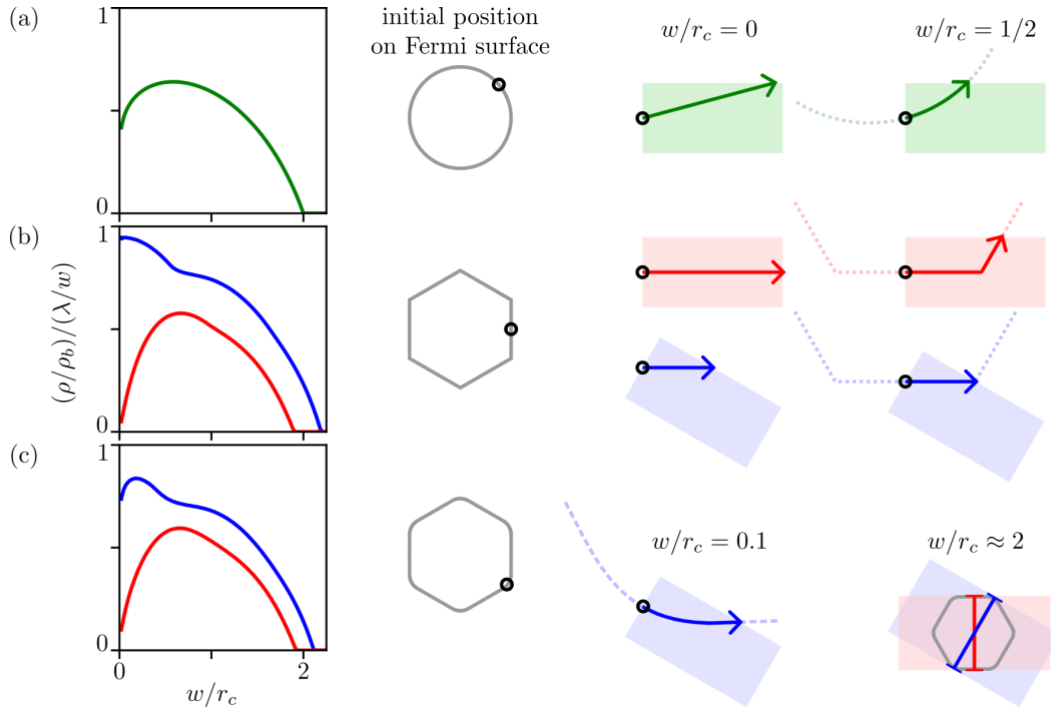


Figure 4. Boltzmann calculations and illustrations of low-field behaviour in the limit of no bulk scattering. We plot the dimensionless ratio $(\rho/\rho_b)/(\lambda/w)$ where ρ_b is the bulk resistivity in zero field. (a) For a circular Fermi surface, the resistivity shows a peak at $w/r_c \approx 0.55$ as the magnetic field bends electrons towards the sample's edges. (b) For a hexagonal Fermi surface, at low magnetic fields with $0 < w/r_c < 1/2$, the magnetic field enhances edge scattering more strongly in the easy direction than in the hard direction. The easy orientation shows a large field-induced resistivity enhancement, whereas the resistivity in the hard orientation is monotonically decreasing. (c) Moving to a realistic Fermi surface for PdCoO₂ introduces an initial resistivity increase in the hard orientation at the lowest magnetic fields. This arises from states near the rounded corners of the Fermi surface, which avoid the edges at zero field but are bent toward them by relatively weak fields. The direction-dependent position at which the resistivity reaches zero near $w/r_c = 2$ reflects additional details of the realistic Fermi surface geometry: for a given magnetic field, a wider channel is needed to accommodate a closed cyclotron orbit in the hard orientation than in the easy orientation.

The low-field regime, defined by $w/r_c < 2$ and depicted in Fig. 4, is mainly characterized by resistivity enhancement from field-induced boundary scattering. The theoretically-expected behavior for an isotropic Fermi surface has previously been established [30,36]. Its main low-field feature is a peak at $w/r_c \approx 0.55$ as electrons are bent towards the boundaries, which is reproduced by our Boltzmann calculation for a circular Fermi surface (Fig. 4a). However, it is clear that this model is insufficient for describing the direction-dependent changes in the qualitative form of the magnetoresistance seen in our data.

This motivates examining the influence of a nearly hexagonal Fermi surface geometry. The effect of Fermi surface geometry and orientation in PdCoO₂ on boundary scattering at zero magnetic field was established in Ref. [22]. In the hard orientation, electrons are always oriented toward the boundaries. In the easy orientation, a substantial fraction of electrons is oriented along the direction of the channel and avoids boundary scattering.

Our data show a much larger field-induced resistivity enhancement in the easy direction than in the hard direction. This can be understood qualitatively by considering the difference between zero-field and low-field trajectories for a perfectly hexagonal Fermi surface, as shown in Fig. 4b. For the easy orientation, the trajectories that avoid boundary scattering at

zero field are oriented toward the boundaries once even a small field is introduced. This creates a peak similar to that for a circular Fermi surface, but of even greater magnitude. On the contrary, for the hard orientation, a small field makes little to no difference as to whether trajectories reach the boundaries. This results in the absence of a low-field peak.

The above picture, based on an idealized hexagonal Fermi surface, misses another prominent feature of our data in the low-field regime: the small, narrow peak in the hard orientation visible for $w/r_c < 1/2$. This peak is reproduced by a calculation using a realistic Fermi surface parameterization based on ARPES measurements [41], as shown in Fig. 4c. This suggests that the peak occurs as electrons near the rounded corners of the Fermi surface are bent toward the boundaries by the magnetic field. Finally, our calculations show that the systematic difference in the value of the B_1 kink in our data between the two orientations reflects a further detail of Fermi surface geometry (Fig. 4c, right): in one orientation, the kink position is set by the corner-to-corner dimension of the Fermi surface, while in the other, the kink position is set by the edge-to-edge dimension of the Fermi surface.

While our calculations do not account for the role of bulk scattering, our data show that it has a large effect. The peak positions appear to be determined by w/r_c , however Fig. 2 demonstrates that the peak magnitudes are strongly dependent on λ/w . Since bulk scattering events interrupt the semi-classical electron trajectories, one would expect that the magnetic field would be more effective at inducing additional boundary scattering if there are fewer bulk scattering events. This is in line with the trend seen in the data.

Interestingly, we have identified that the easy-orientation peak is dominated by electrons at the edges of the Fermi surface, whereas the hard-orientation peak is dominated by electrons at the corners of the Fermi surface. This offers the opportunity to separately study scattering at the edges and corners of the Fermi surface. Previous work on PdCoO_2 has suggested that scattering at the edges and corners may differ, and that this difference may be instrumental in explaining several unconventional bulk transport properties [6]. If suitable theory is developed, our data may allow for a quantitative determination of any potential in-plane scattering anisotropy.

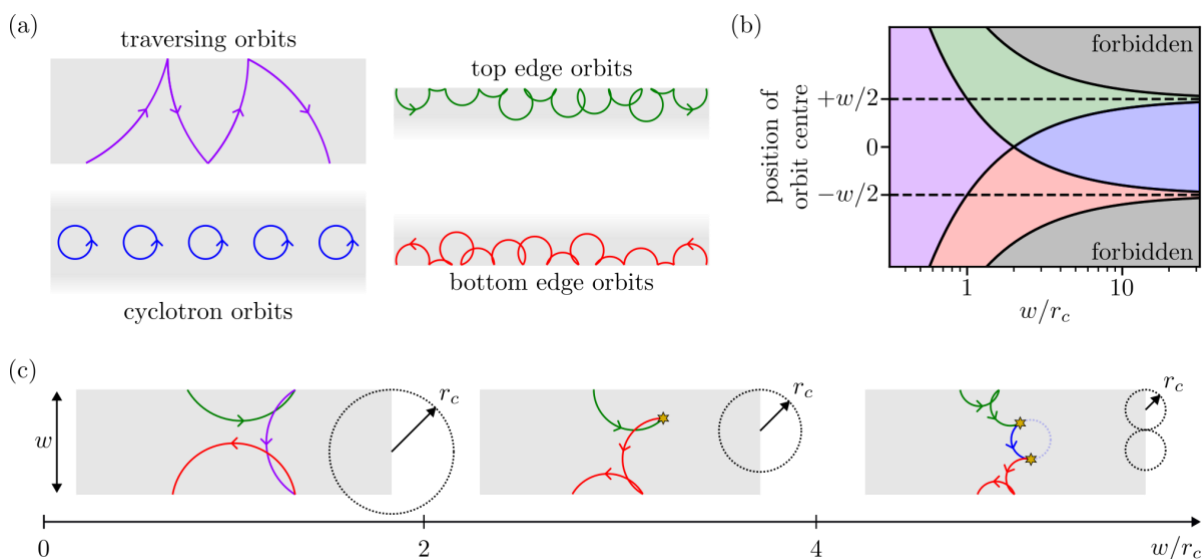


Figure 5. (a) Illustration of different orbit types. Orbits can be classified by whether they interact with one edge, both, or neither. For $w/r_c < 2$, the sample supports traversing orbits, making contact with both edges. For $w/r_c > 2$, the sample supports closed cyclotron orbits, making contact with neither edge. At all fields, the sample supports edge orbits. These orbits start and end at the same edge, and travel in opposite directions at opposite edges. (b) Illustration of the phase space for each orbit type as a function of w/r_c . The plot indicates the possible positions of the orbit centre (the hypothetical centre point of the closed orbit) relative to the channel's boundaries, marked by dashed lines. (c) Depiction of routes to inter-edge scattering, which is necessary for width-dependent magnetoresistance. For $w/r_c < 2$, no bulk scattering is required for inter-edge scattering. For $2 < w/r_c < 4$, at least one bulk scattering event is required. For $w/r_c > 4$, at least two bulk scattering events are required.

The features of the high-field regime, defined by $w/r_c > 2$ and depicted in Fig. 5, can be understood by considering the possible types of orbits in a finite-width sample as a function of w/r_c . For simplicity, we consider a circular Fermi surface, though the same reasoning applies to the real Fermi surface of PdCoO₂. As depicted in Fig. 5a, one can delineate four types of orbits [42]: (1) traversing orbits, touching both boundaries, (2) cyclotron orbits, touching neither boundary, and (3), (4) top and bottom edge orbits, touching one boundary or the other. Simple geometry allows for constructing a phase diagram (Fig. 5b) for the possible locations of each orbit type relative to the channel.

In the typical, hypothetical picture of a bulk magnetoresistance measurement, one ignores the presence of sample boundaries, and assumes that the bulk magnetoresistance arises only from cyclotron orbits. On the other hand, a size-dependent contribution to the magnetoresistance, scaling as w/r_c , must necessarily arise from trajectories interacting with both sample boundaries. Measurements in Ref. [6] show that bulk magnetoresistance is a weak effect in PdCoO₂—below 15% at a temperature of 2 K and a magnetic field of 9 T. While the slight positive magnetoresistance visible in Fig. 2 at high fields in our widest samples is likely attributable to a bulk contribution, the dominant features in our data scale as w/r_c and are therefore attributable to a size-dependent contribution.

Therefore, to understand the size-dependent signal, we must consider trajectories interacting with both boundaries. At fields with $w/r_c < 2$, traversing orbits connect the two boundaries, as shown in Fig. 5c (left). Once $w/r_c > 2$, traversing orbits no longer exist. The only way for an electron to travel between boundaries is via a trajectory involving at least one bulk scattering event, transferring an electron between top and bottom edge orbits (Fig. 5c, middle). Once $w/r_c > 4$, a trajectory between top and bottom edge orbits must involve an intermediate cyclotron orbit, and therefore requires at least two bulk scattering events (Fig 5c, right). The change in the number of required bulk scattering events for inter-edge scattering at $w/r_c = 2$ and $w/r_c = 4$ are the origin of the B_1 and B_2 kinks identified in the data.

While the discussion so far has focussed on the ratio of width w to cyclotron radius r_c , the length scale(s) associated with bulk scattering also play a role. For a sample with $\lambda \gg w$, an electron will scatter only rarely as it traverses a channel, and so the bulk collisions required for a size-dependent signal for $w/r_c > 2$ are rare. This suppresses the magnetoresistance in this regime, explaining the sharp kinks seen in our data in the narrower channels. For $\lambda < w$, an electron is likely to scatter as it traverses a channel, and it is not difficult to fulfill the requirement for a size-dependent signal. This is reflected in the absence of resolvable kinks in our data for the widest channels.

It is interesting to note that for any absolute channel width, one would eventually expect a complete suppression of boundary-induced resistance at high enough magnetic field. This should occur for two reasons: (1) in the limit that $r_c \ll w$, the majority of electrons occupy cyclotron orbits, and (2) in the limit that $r_c \ll \lambda$, for those electrons remaining in edge orbits, the bulk scattering necessary to undergo inter-edge scattering is greatly suppressed [43]. Especially in a material with small and saturating bulk magnetoresistance, this implies the opportunity for a sizeable negative magnetoresistance in channels with significant zero-field boundary-induced resistance.

While we have discussed the effect of bulk scattering within the framework of momentum-relaxing scattering events that randomize an electron's momentum, we cannot rule out the presence of small viscous corrections to the observed data. As described recently [10,44], such corrections are visible in microwave spectroscopy experiments on oriented PdCoO₂ crystals. Their microscopic origin is thought to be small angle scattering from extended impurity potentials, a phenomenon which would also be present in the devices studied here. Searching for their effect on magnetotransport would likely require Boltzmann transport modelling including an applied magnetic field and a realistic parameterization of the PdCoO₂ Fermi surface. Such a calculation presents significant technical difficulties, and to our knowledge no code to perform it currently exists. Until it does, it is unlikely to be possible to identify and quantify small viscous contributions to data such as those presented here.

In conclusion, we have presented a comprehensive data set describing directional finite-size magnetotransport in oriented conducting channels FIB sculpted from single crystals of delafossite metals. Our work illustrates the utility of finite-size magnetotransport. By tuning cyclotron radius relative to sample width, we were able to concretely relate features of our dataset to geometrical properties of the Fermi surface. By tuning both of these length scales relative to intrinsic scattering lengths, we were able to measure the effect of bulk scattering in significantly more detail than possible in a conventional transport measurement. At the moment, appropriate theory for quantitatively assessing the role of scattering has not yet been developed. We hope to motivate such theoretical work, enabling quantitative insights to be taken from our data set. We hope that the extensiveness and quality of our data set, as well as the insights obtained from it, serve as a benchmark and motivation for future work.

Methods

Extraction of magnetoresistance data

The raw voltage values V were converted to the resistivity ρ based on the dimensions of the sample, width w , thickness t and average contact separation L , and the applied current I through the relation $\rho = \frac{Vwt}{IL}$. This resistivity was subsequently interpolated, averaged over the decreasing and increasing magnetic field sweeps, and symmetrized.

The voltage measurements used excitation currents in the range 1mA to 9mA. Linearity of the current-voltage measurements was checked before each measurement and no signs of non-linearities were observed.

Determination of bulk mean free path and average cyclotron radius

The bulk momentum relaxing mean free path L_{MR} was calculated based on the in-plane resistivity of the widest studied channel at 5K temperature, ρ_{bulk} , 25.8 n Ω cm for PdCoO₂ and 31.8 n Ω cm for PtCoO₂ obtained as the average of the resistivity of the easy and hard channels at zero magnetic field. The calculation used the standard 2D expression, $\lambda = \frac{e^2 \bar{k}_F}{h d \rho_{\text{bulk}}} \frac{1}{[45]}$, where e is the electron charge, h is the Planck constant, $d = 17.743/3$ Å for PdCoO₂ and 17.808/3 Å for PtCoO₂, $\bar{k}_F = 0.9518$ Å⁻¹ for PdCoO₂ and 0.9542 Å⁻¹ for PtCoO₂ are the angle averaged Fermi momenta $\bar{k}_F \equiv \frac{1}{2\pi} \int_0^{2\pi} d\theta k_F(\theta)$ based on parameters from Ref. [41]. This averaged value was also used to determine the cyclotron radius r_c used throughout the main text.

Focused ion beam microstructure fabrication

Details of the FIB micro-structuring are described elsewhere [20,46]. The FIB microstructures contain current homogenization meanders ensuring current has dispersed through the thickness following a top contact injection. The large ab -plane to c -axis resistivity anisotropy means current preferentially flows through the top layers and estimating the resistivity based on the full thickness would overestimate resistivity. The meander extends the current path through the sample and allows for proper current homogenization. The approximate length of the meander needed for current homogenization can be estimated considering current diffusion from the top layers as

$$L_{\text{meander}} \sim t \sqrt{\frac{\rho_c}{\rho_{ab}}}.$$

To achieve precise geometry of the narrowed channels and accurate width measurement, careful alignment and a uniform cross-section were essential. A cross-shaped marker aligned along the easy direction helped ensure the channel edges were parallel within 0.1°. Narrowing was performed iteratively, using low polishing currents in range 0.17 nA to 0.79 nA to minimize beam tail damage and edge rounding. For channels narrower than 5 μm , the sides were narrowed from a different side in each iteration since the width by which the channel was narrowed became typically sub-micrometer. The channel width was determined by measuring the widest point (w_{outer}) and the undamaged top surface width (w_{inner}), then calculating a weighted average $w = (w_{\text{inner}} + 2 w_{\text{outer}})/3$ to account for the rounded edges resulting from beam tail effects.

Single crystal growth

Details are given elsewhere for the crystal synthesis of PdCoO₂ [20] and PtCoO₂ [17].

Acknowledgments

M.M thanks Kent Shirer for insightful help with the micro-structure fabrication. This project was supported by the Max Planck Society and the European Research Council (ERC) under the European Union's Horizon 2020 research and innovation programme (MiTopMat, grant agreement no. 715730). M.D.B. acknowledges EPSRC for PhD studentship support through grant number EP/L015110/1. A.S. would like to thank Zack Gomez and Edwin Huang for helpful discussions and Tom Devereaux for letting us use his group cluster. Computational work was performed on the Sherlock cluster at Stanford University and on resources of the National Energy Research Scientific Computing Center, supported by DOE under contract DE_AC02-05CH11231.

References

- [1] D. B. Rogers *et al.*, *Inorg Chem* **10**, 723 (1971).
- [2] A. P. Mackenzie, *Reports on Progress in Physics* **80**, 32501 (2017).
- [3] C. W. Hicks *et al.*, *Phys Rev Lett* **109**, 116401 (2012).
- [4] H. Takatsu *et al.*, *Phys Rev Lett* **111**, 056601 (2013).
- [5] N. Kikugawa *et al.*, *Nat Commun* **7**, 10903 (2016).
- [6] N. Nandi *et al.*, *NPJ Quantum Mater* **3**, 66 (2018).
- [7] E. Zhakina *et al.*, *Proc Natl Acad Sci U S A* **120**, e2307334120 (2023).
- [8] Y. Zhang *et al.*, *Nat Commun* **15**, 1399 (2024).
- [9] V. Sunko *et al.*, *Phys Rev X* **10**, 021018 (2020).
- [10] G. Baker *et al.*, *Phys Rev X* **14**, 011018 (2024).
- [11] J. M. Ok *et al.*, *Phys Rev Lett* **111**, 176405 (2013).
- [12] C. W. Hicks *et al.*, *Phys Rev B* **92**, 014425 (2015).
- [13] F. Arnold *et al.*, *Phys Rev B* **101**, 195101 (2020).
- [14] H.-J. Noh *et al.*, *Phys Rev Lett* **102**, 256404 (2009).
- [15] J. A. Sobota *et al.*, *Phys Rev B* **88**, 125109 (2013).
- [16] H. J. Noh *et al.*, *Sci Rep* **4**, 2 (2014).
- [17] P. Kushwaha *et al.*, *Sci Adv* **1**, 1500692 (2015).
- [18] V. Sunko *et al.*, *Nature* **549**, 492 (2017).
- [19] V. Sunko *et al.*, *Sci Adv* **6**, eaaz06117 (2020).
- [20] M. D. Bachmann *et al.*, *Nat Commun* **10**, 5081 (2019).
- [21] C. Putzke *et al.*, *Science* (1979) **368**, 1234 (2020).
- [22] M. D. Bachmann *et al.*, *Nat Phys* **18**, 819 (2022).
- [23] P. H. McGuinness *et al.*, *Proc Natl Acad Sci U S A* **118**, 2113185118 (2021).
- [24] E. Zhakina *et al.*, *Phys Rev B* **107**, 094203 (2023).
- [25] M. D. Bachmann, *Manipulating Anisotropic Transport and Superconductivity by Focused Ion Beam Microstructuring* (2019).
- [26] C. Q. Cook and A. Lucas, *Phys Rev B* **99**, 235148 (2019).
- [27] D. Valentinis *et al.*, *Phys Rev Res* **5**, 013212 (2023).
- [28] G. Baker, D. Valentinis, and A. P. Mackenzie, *Low Temperature Physics* **49**, 1338 (2023).
- [29] D. MacDonald and K. Sarginson, *Proceedings of the Royal Society A* **203**, 223 (1950).
- [30] E. Ditlefsen and J. Lothe, *Philosophical Magazine* **14**, 759 (1966).
- [31] P. S. Alekseev, *Phys Rev Lett* **117**, 166601 (2016).
- [32] T. Scaffidi *et al.*, *Phys Rev Lett* **118**, 226601 (2017).
- [33] P. S. Alekseev and M. A. Semina, *Phys Rev B* **98**, 165412 (2018).
- [34] P. S. Alekseev and M. A. Semina, *Phys Rev B* **100**, 125419 (2019).
- [35] T. Holder *et al.*, *Phys Rev B* **100**, 245305 (2019).
- [36] O. E. Raichev *et al.*, *Phys Rev B* **101**, 235314 (2020).
- [37] S. Masubuchi *et al.*, *Phys Rev Lett* **109**, 1 (2012).
- [38] T. Thonton *et al.*, *Phys Rev Lett* **63**, 2128 (1989).
- [39] G. M. Gusev *et al.*, *Phys Rev B* **98**, 161303(R) (2018).
- [40] P. J. W. Moll *et al.*, *Science* (1979) **351**, 1061 (2016).
- [41] V. Sunko, *Angle Resolved Photoemission Spectroscopy of Delafossite Metals*, University of St Andrews, 2019.
- [42] C. W. J. Beenakker, H. van Houten, and B. J. van Wees, *Superlattices Microstruct* **5**, 127 (1989).
- [43] M. Büttiker, *Phys Rev B* **38**, 9375 (1988).

- [44] G. Baker, M. Moravec, and A. P. Mackenzie, *Ann Phys* **536**, 2400087 (2024).
- [45] J. M. Ziman, *Principles of the Theory of Solids* (1964).
- [46] P. J. W. Moll, *Annu Rev Condens Matter Phys* **9**, 147 (2018).
- [47] E. H. Sondheimer, *Adv Phys* **1**, 1 (1952).